Hybrid model calculations of direct photons in high-energy nuclear collisions

Bjørn Bäuchle[1,2,*] and Marcus Bleicher[2]

[1] *Frankfurt Institute for Advanced Studies, Frankfurt am Main, Germany*
[2] *Institut für Theoretische Physik, Goethe-Universität, Frankfurt am Main, Germany*

Direct photon emission in heavy-ion collisions is calculated within the relativistic micro+macro hybrid model and compared to the microscopic transport model UrQMD. In the hybrid approach, the high-density part of the evolution is replaced by an ideal 3-dimensional hydrodynamic calculation. This allows to examine the effects of viscosity and full local thermalization, juxtaposing the transport model to the ideal fluid-dynamics. We study the origin of high-$p_\perp$ photons as well as the impact of elementary high-$\sqrt{s}$ collisions. We study the contribution of different production channels and non-thermal radiation to the spectrum of direct photons. Detailed comparison to the measurements by the WA 98-collaboration are also undertaken.

I. INTRODUCTION

Creating and studying high-density and -temperature nuclear matter is the major goal of heavy-ion experiments. A state of quasi-free partonic degrees of freedom, the Quark-Gluon-Plasma (QGP) [1, 2] may be formed, if the energy density in the reaction is high enough. Strong jet quenching, high elliptic flow and other observations made at the Relativistic Heavy Ion Collider (BNL-RHIC) suggest the successful creation of a strongly coupled QGP (sQGP) [3–6]. Possible evidence for the creation of this new state of matter has also been put forward by collaborations at the Super Proton Synchrotron (CERN-SPS), as for instance the step in the mean transverse mass excitation function of protons, kaons and pions and the enhanced K^+/π^+-ratio [7].

Out of the many possible observables, electromagnetic probes have the advantage of leaving the hot and dense region undisturbed: once they are created, they escape freely from the reaction zone, due to their negligible rescattering cross-sections. Besides dileptons, direct photon emission is therefore of greatest interest to gain insight into the early, hot and therefore possibly partonic stages of a reaction. Direct photons are distinguished from the bulk of photons as those coming from collisions and not decays.

Unfortunately, the overwhelming amount of photons in heavy-ion collisions comes from hadronic decays in the late stages, mostly $\pi^0 \to \gamma\gamma$. These decay-photons impose a serious challenge for the experimental extraction of direct photon data. Up to now, several experiments have gone through the challenge to obtain the spectra of direct photons: Helios, WA 80 and CERES (all at CERN-SPS) could publish upper limits, while WA 98 (CERN-SPS) and PHENIX (BNL-RHIC) have published data points for direct photons.

On the theoretical side, calculations for the elementary photon production processes are known since long, see e.g. Kapusta *et al.* [8] and Xiong *et al.* [9]. The major problem here is the difficulty to describe the time evolution of the produced matter. Up to now, this is not possible from first principle Quantum Chromodynamics (QCD), one has to rely on well-developed dynamical models to describe the space-time evolution of the nuclear interactions in the hot and dense stage of the reaction. One of the existing approaches to those models is relativistic transport theory [10–15]. In this kind of microscopic description, the hadronic and/or partonic stage of the collision is described under certain approximations. Most transport models, for instance, cannot describe collisions with more than two incoming particles, which restricts the applicability to low particle densities, where multi-particle interactions are less important. Some attempts to include multi-particle interactions do exist [13, 16–19], but this field of study is still rather new. The coupling of a partonic phase with a hadronic phase imposes one more problem on transport models, because the microscopic details of that transition are not well known. Another caveat in the transport approach is that all microscopic scatterings are explicitly treated in the model and therefore the cross-sections for all processes must be known or extrapolated. However, for many processes high quality experimental data are not available, and therefore a large fraction of the cross-sections have to be calculated or parametrized by additional models.

Relativistic, non-viscous, perfect fluid- or hydrodynamics is a different approach to explore the space-time evolution of a heavy-ion collision [20–24]. It constitutes a macroscopic description of the matter that is created, assuming that at every time and in every place the matter is in local thermal equilibrium. This assumption can only be true if the matter is sufficiently dense, so in the late stages of a heavy-ion collision fluid-dynamics looses applicability. In addition, the requirement of local thermal equilibrium restricts the starting time of the hydrodynamic model. An advantage is that in the dense stages, hydrodynamics can propagate any kind of matter, and also allows for transitions between two types of matter, e.g. QGP and hadron gas, if an appropriate Equation of State (EoS) is provided. Fluid-dynamics can therefore be used to study hadronic and partonic matter in one

*Electronic address: baeuchle@th.physik.uni-frankfurt.de

common model.

The restrictions of this kind of model can be loosened as well. By introducing viscosity and heat conductivity, perfect thermal equilibrium does not have to be present at any point. However, even with second order corrections the matter has to be close to equilibrium [25–27]

Input to solve the hydrodynamic differential equations are the boundaries, i.e. the initial state (the distributions of all relevant densities and currents at the time the evolution starts), the Equation of State providing the pressure as function of the energy and baryon densities, that describes the behaviour of the matter that is considered, and the freeze-out hypersurface.

Finally, approaches to the theoretical description of direct photon spectra may include calculations with perturbative Quantum-Chromo-Dynamics (pQCD). Calculations based on pQCD describe the photon data in proton-proton collisions very well and, if scaled by the number of binary collisions, also those in heavy-ion reactions. The range of applicability is limited to high transverse momenta $p_\perp^\gamma \gg 1$ GeV.

The different approaches have different applicability limits. E.g., thermal rates can only be applied if the assumption of local thermal equilibrium is fulfilled. Photon emission rates can then be calculated by folding the particle distribution functions of the participating particle species with the respective cross-sections. This framework can be applied to either static models, simplified hydrodynamics-inspired models such as the blast wave model and to full fluid-dynamic calculations. The space-time evolution of a reaction as predicted by microscopic theories can be averaged over in order to apply thermal rates to the coarse-grained distributions [22]. The application of microscopic cross-sections can only be undertaken in a model where all microscopic collisions are known. That limits the field of use to transport models. There have been several calculations for photon spectra from transport models [28, 29]

In this paper, we investigate the spectra of direct photons coming from microscopic hadronic scatterings, thermal hadronic and partonic emission and hard initial pQCD scatterings. We compare results from a purely microscopic model to those from an integrated micro+macro hydrodynamic approach that embeds a hydrodynamic phase in the UrQMD approach. The paper is organized as follows. First, we explain the hybrid model (Section II). In the following Section III, we elaborate on the photon sources considered in our model. In Section IV, we apply our model to compare thermal rates from microscopic theory to those from the literature, compare different physics assumptions with experimental data from the WA98 collaboration [30] and analyse the sources of photon emission.

II. THE HYBRID MODEL

UrQMD v2.3 (Ultra-relativistic Quantum Molecular Dynamics) is a microscopic transport model [10, 11]. It includes all hadrons and resonances up to masses $m \approx 2.2$ GeV and at high energies can excite and fragment strings. The cross-sections are either parametrized, calculated via detailed balance or taken from the additive quark model (AQM), if no experimental values are available. At high parton momentum transfers, PYTHIA [31] is employed for pQCD scatterings. In the UrQMD framework, propagations and spectral functions are calculated as in vacuum. UrQMD has been used by Dumitru *et al.* to study direct photon emission earlier [28].

In the following, we compare results from the microscopic model to results obtained with the hybrid model description [32]. Here, the high-density part of the reaction is modelled using ideal 3+1-dimensional fluid-dynamics. The unequilibrated initial state and the low-density final state are described by UrQMD. To connect the initial phase with the high-density phase, the baryon-number-, energy- and momentum-densities are smoothed and put into the hydrodynamic calculation after the incoming nuclei have passed through each other. In non-central collisions, the spectators are propagated in the cascade. After the local rest frame energy density has dropped below a threshold value of $\epsilon_{\rm crit} = 730$ MeV/fm^3 ($\approx 5\epsilon_0$), particles are created on an isochronous hyper-surface from the densities by means of the Cooper-Frye formula and propagation is continued in UrQMD. The transition scenario chosen for the present studies is always isochronous, i.e. the whole system must meet the criterion at the same calculational frame-time before freeze-out is performed. Earlier investigations within this model include an extensive analysis of the effect of changing the transition criteria [32], strangeness production [33, 34], HBT correlations [35], transverse mass [36] and elliptic flow [37].

For the investigation presented here, different Equations of State are used for the hydrodynamic phase. The base line calculations are done with a hadron gas Equation of State (HG-EoS), which includes the same degrees of freedom also present in the transport phase. This allows to explore the effects due to the change of the kinetic description. Secondly, we use a MIT-Bag Model EoS (BM-EoS) with a partonic phase and a first order phase transition [20]. We use the BM-EoS for investigations of photon emission from the QGP.

III. PHOTON EMISSION SOURCES

Photon emission is calculated perturbatively in both models, hydrodynamics and transport, because the evolution of the underlying event is not altered by the emission of photons due to their very small emission probability. The channels considered for photon emission may differ between the hybrid approach and the binary

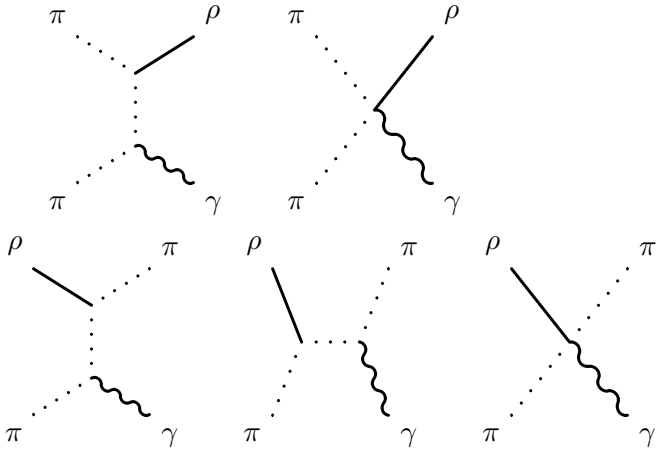

FIG. 1: Some of the Feynman diagrams taken into account for the calculation of cross-sections (taken from [8])

scattering model. Emission from a Quark-Gluon-Plasma can only happen in the hydrodynamic phase, and only if the equation of state used has partonic degrees of freedom. Photons from baryonic interactions are neglected in the present calculation. Emission of hard photons from early pQCD-scatterings of nucleons is calculated separately and incoherently added to the simulated spectra.

A. Photons from microscopic collisions

In the transport part of the (hybrid) model, each scattering is examined and the cross-section for photon emission is calculated. Here, we employ the well-established cross-sections from Kapusta *et al.* [8] and Xiong *et al.* [9]. Kapusta and collaborators based their calculations on the photon self-energy derived from a Lagrange density involving the pion, rho and photon-fields

$$\mathcal{L} = |D_\mu \Phi|^2 - m_\pi^2 |\Phi|^2 - \frac{1}{4}\rho_{\mu\nu}\rho^{\mu\nu} + \frac{1}{2}m_\rho^2 \rho_\mu \rho^\mu - \frac{1}{4}F_{\mu\nu}F^{\mu\nu} \quad . \tag{1}$$

Here, Φ is the pion field, $\rho_{\mu\nu} = \partial_\mu \rho_\nu - \partial_\nu \rho_\mu$ and $F_{\mu\nu} = \partial_\mu A_\nu - \partial_\nu A_\mu$ are the ρ and photon field-strength tensors and $D_\mu = \partial_\mu - \imath e A_\mu - \imath g_\rho \rho_\mu$ is the covariant derivative. The ρ decay constant g_ρ is calculated from the total width Γ^ρ_{tot} of the ρ meson:

$$g_\rho^2 = 48\pi \frac{\Gamma^\rho_{\text{tot}} m_\rho^2}{\left(\sqrt{m_\rho^2 - 4m_\pi^2}\right)^3} \quad . \tag{2}$$

The cross-sections calculated correspond to the Feynman diagrams shown in Figure 1.

The differential cross-sections used for the present investigation [8, 9] are given in the Appendix A.

All scatterings that happen during the transport phase are examined in order to obtain direct photon spectra. For every scattering that may produce photons (i.e. those that have initial states equal to the processes listed in Appendix A), the corresponding fraction of a photon,

$$N_\gamma = \frac{\sigma_{\text{em}}}{\sigma_{\text{tot}}} \quad , \tag{3}$$

is produced. Here, σ_{tot} is the sum of the total hadronic cross-section for a collision with these ingoing particles (as provided by UrQMD) and the electromagnetic cross-section σ_{em} as calculated by the aforementioned formulæ. In order to obtain the correct angular distribution of the produced photons and to enhance statistics, for each scattering many fractional photons are created that populate all kinematically allowed momentum transfers t

$$\Delta N_\gamma^{\text{t}} = \frac{\frac{d\sigma_{\text{em}}}{dt}(s,t)\Delta t}{\sigma_{\text{tot}}(s)} \quad , \tag{4}$$

and are distributed evenly in the azimuthal angle φ. The integral $\sigma_{\text{em}}(s) = \int {}^{d\sigma_{\text{em}}}/_{dt} dt$ is performed analytically for each channel. The resulting formulæ are shown in appendix B.

Since the width of the rho-meson is not negligible, its mass distribution should be taken into account. For the processes with a rho-meson in the initial state, the actual mass $m_\rho = \sqrt{p_\mu p^\mu}$ of the incoming meson is used for calculation of the cross-section. If there is a rho-meson in the final state, then first the outgoing mass is chosen randomly according to a Breit-Wigner distribution with mass-dependent width. This mass is then used for all further calculations of this process.

Figure 2 shows the cross-sections of the channels listed above as a function of $\sqrt{s}$.

B. Photons from hydrodynamics

In the hydrodynamic phase photons are produced fractionally from every cell of the calculation whose energy density is above a threshold $\varepsilon_{\text{thr}} = 10^{-12}\ \varepsilon_0$. We use the parametrizations by Turbide, Rapp and Gale [38]. They use an effective non-linear σ-model Lagrange density in which the vector and axial vector fields are implemented as massive gauge fields of the chiral $U(3)_L \times U(3)_R$ symmetry to obtain the rates. For details on this ansatz, the reader is referred to the original publication [38].

As mentioned earlier, the processes calculated by Turbide *et al.* differ from those considered by Kapusta *et al.* Only the processes $\pi\pi \to \gamma\rho$ and $\pi\rho \to \gamma\pi$ are therefore common in both models. Their rate for $\pi\rho \to \gamma\pi$ directly includes the process with an intermediate a_1-meson.

All parametrizations follow the general form

$$E\frac{dR}{d^3p} = A \exp\left(\frac{B}{(2ET)^C} - D\frac{E}{T}\right) \quad , \tag{5}$$

where A, B, C and D are linear functions of some power of the temperature T: $A(T) = A_1 + A_2 T^{A_3}$. Table I depicts the full parameter set. In the rates, the energy E

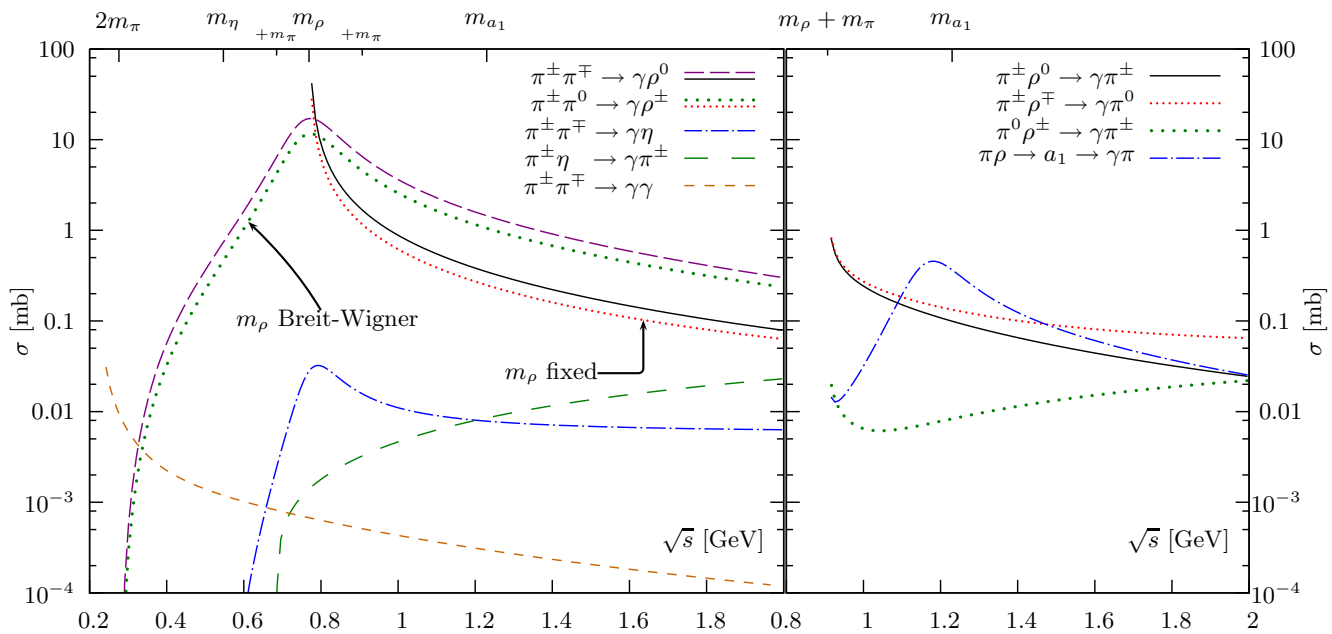

FIG. 2: (Color Online.) Cross-sections for all included channels as a function of $\sqrt{s}$. For visibility, the cross-sections for all processes $\pi\rho \to \gamma\pi$ are shown separately. They have been calculated with a rho mass $m_\rho = 0.769$ GeV. The left plot shows the cross-sections for $\pi\pi \to \gamma\rho$ both for fixed rho mass ($m_\rho = 0.769$ GeV, labelled "m_ρ fixed") and for variable rho mass (labelled "m_ρ Breit-Wigner").

and temperature T are to be given in units of GeV, and the result will have the unit GeV^{-2} fm^{-4}. Following [39] and [40], we introduce a hadronic form-factor according to

$$F(\bar{t}) = \left(\frac{2\Lambda^2}{2\Lambda^2 - \bar{t}}\right)^2 \quad , \tag{6}$$

which enters the rates quadrupled. Here, $\Lambda = 1$ GeV is taken to be the typical hadronic scale and $\bar{t}$ the average momentum transfer $\bar{t} = -2Em_X$, with X being the meson that is exchanged in the t-channel (see Table I, last column).

In the Quark-Gluon-Plasma, the rate used is taken from Ref. [41]. They computed the full leading-order result as

$$E\frac{dR}{d^3p} = \sum_{i=1}^{N_f} q_i^2 \frac{\alpha_{\rm em}\alpha_{\rm S}}{2\pi^2} T^2 \frac{1}{e^x+1}\left(\ln\left(\frac{\sqrt{3}}{g}\right) + \frac{1}{2}\ln(2x) + C_{22}(x) + C_{\rm brems}(x) + C_{\rm ann}(x)\right) \tag{7}$$

and give convenient parametrizations for the contribution of $2 \leftrightarrow 2$-, bremsstrahlung- and annihilation-processes (C_{22}, $C_{\rm brems}$ and $C_{\rm ann}$, respectively)

$$C_{22}(x) = 0.041x^{-1} - 0.3615 + 1.01\exp(-1.35x) \tag{8a}$$

$$C_{\rm brems}(x) + C_{\rm ann}(x) = \sqrt{1+\frac{N_f}{6}}\left[\frac{0.548\ln\left(12.28+\frac{1}{x}\right)}{x^{\frac{3}{2}}} + \frac{0.133x}{\sqrt{1+\frac{x}{16.27}}}\right] \quad . \tag{8b}$$

In Equations (7) and (8), $x = E/T$, q_i is the charge of quark-flavour i, $\alpha_{\rm em}$ and $\alpha_{\rm S} = g^2/4\pi$ are the electromagnetic and QCD coupling constants, respectively. In our calculations, we use $N_f = 3$, and therefore $\sum_i q_i^2 = 2/3$.

The temperature dependence of $\alpha_{\rm S}$ is taken from [40] as

$$\alpha_{\rm S}(T) = \frac{6\pi}{(33-2N_f)\ln\left(\frac{8T}{T_C}\right)} \tag{9}$$

Process	A_1	A_2	A_3	B_1	B_2	B_3	C_1	C_2	C_3	D_1	D_2	D_3	Exchange
$\pi\pi \to \gamma\rho$	0.0	1.0	-5.0	5.328	-9.314	-0.584	-0.088	0.0	–	0.8998	-0.3189	0.721	π
$\pi\rho \to \gamma\pi$	0.0	1.0	2.8	-0.727	-1.461	2.3094	0.86	0.0	–	0.9957	-0.566	1.4094	π
$\pi K^* \to \gamma K$	0.0	1.0	3.75	-0.35	0.0	–	1.05	0.0	–	3.2222	-2.2893	0.03435	K
$\pi K \to \gamma K^*$	0.0	1.0	-3.0	1.51	-5.4018	-0.6864	-0.07	0.0	–	0.91	0.0	–	K
$\rho K \to \gamma K$	0.0	1.0	3.5	-0.634	-0.9386	1.551	1.01	0.0	–	1.164	-0.568	0.5397	K
$K^* K \to \gamma\pi$	0.0	1.0	3.7	-1.0299	-6.096	1.889	0.975	-1.613	2.162	0.96	0.0	–	K

TABLE I: The values used in the parametrizations of the photon emission rates (see text). The last column states which meson is supposed to be transferred in the exchange.

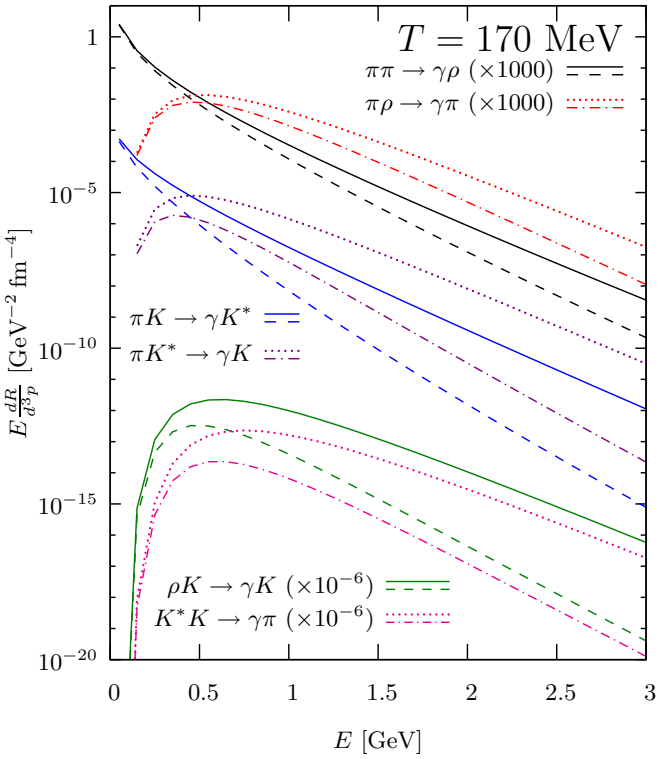

FIG. 3: (Color Online.) Rates of all processes considered in the hydrodynamic phase with a hadron gas EoS with form factor (solid and dotted lines) and without form factor (dashed and dash-dotted lines). For better visibility, some rates have been scaled by factors of 1000 ($\pi\pi \to \gamma\rho$ and $\pi\rho \to \gamma\pi$) and 10^{-6} ($\rho K \to \gamma K$ and $K^* K \to \gamma\pi$), respectively.

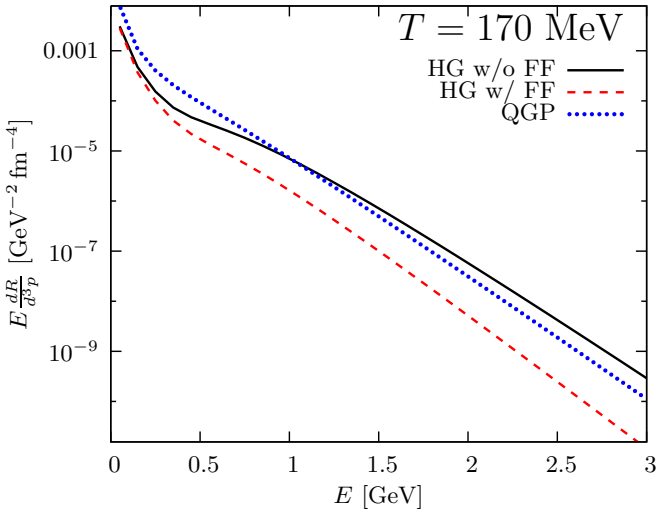

FIG. 4: (Color Online.) Thermal rates: Comparison between the sum of all hadronic contributions shown above (with and without form factor, FF) to the contribution of Quark Gluon Plasma.

and the critical temperature to be $T_C = 170$ MeV.

Figure 3 shows all hadronic rates with and without form factor. In Figure 4, the sum of all hadronic rates is compared to the QGP-rate at $T = 170$ MeV.

C. Photons from primordial pQCD-scatterings

At high transverse momenta, a major contribution to the photon yield is the emission of photons from hard pQCD-scatterings of the partons in the incoming protons. In the intermediate and high $p_\perp$-regions, the contribution may be comparable to or smaller than the yield from other sources.

We apply the data extracted by Turbide *et al.* [38]. They first scale the photon spectrum from proton-proton-collisions by the number of binary collisions in Pb+Pb-collisions, and then add a Gaussian-shaped additional $k_\perp$-smearing to the result. The width of the Gaussian is obtained by fitting this procedure to the data from proton-nucleus collisions. The values shown here are obtained with a $\langle \Delta k_\perp^2 \rangle = 0.2$ GeV^2.

However, the procedure of fitting pQCD-data to proton-nucleus collisions inherently assumes that all photons in those collisions come from pQCD scatterings. However, mesonic interactions may be present in pA-collisions as well. When trying to add the pQCD-spectrum obtained with this method to the spectrum from all mesonic collisions some kind of double-counting may occur.

For comparison, we also show pQCD spectra obtained earlier by Gale [42] following Wang *et al.* [43]. They follow the same procedure as explained above. The authors of [42] obtain a higher intrinsic transverse parton

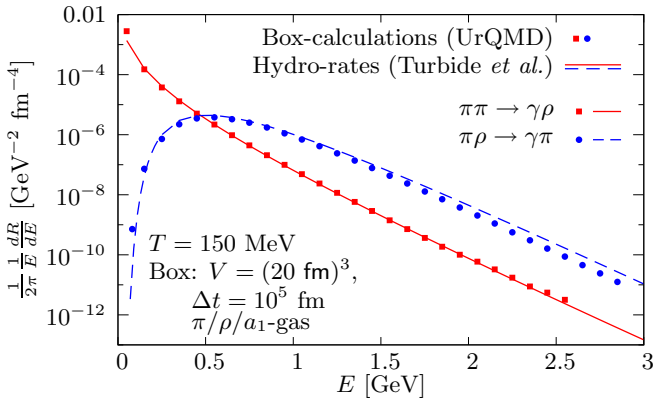

FIG. 5: (Color Online.) Comparisons between the rates from [38] (lines) and box calculations restricted to a π, ρ, a_1-system (points) with UrQMD at $T = 150$ MeV.

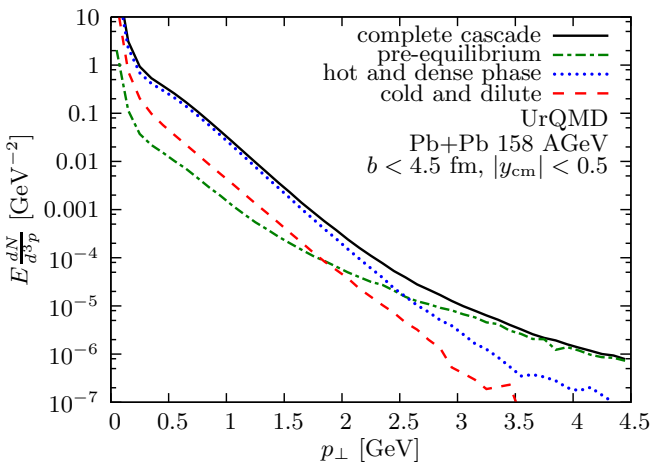

FIG. 6: (Color Online.) UrQMD calculation. Contributions of the phases of pre-equilibrium ($t < t_1 = 1.424$ fm, dash-dotted green line), hot-and-dense ($t_1 < t < t_2 = 13.25$ fm, dotted blue line) and cold-and-dilute ($t_2 < t$, dashed red line) phases to the spectrum from pure cascade calculations (solid black line).

momentum of $\langle \Delta k_\perp^2 \rangle = 0.9$ GeV^2, yet lower spectra.

D. String ends in UrQMD

In UrQMD, the leading particles from a string have a reduced cross-section during their formation time. Scatterings of the string ends happen typically at high center-of-mass energies $\sqrt{s}$. They contribute significantly to the photon spectra at high transverse momenta. Since these particles are not fully formed hadrons, but effectively represent quarks or di-quarks, a hadronic treatment of those processes is questionable. Therefore, we will investigate the contributions from such collisions in Section IV B separately.

IV. RESULTS

A. Rates from transport and hydrodynamics

Before comparing photon spectra from complex nucleus-nucleus collisions between cascade- and hybrid model, we check to see if both approaches give similar results for the relatively simple setup of a fully thermalized box.

I.e., we run UrQMD in a box, allowing only π-, ρ- and a_1-mesons to be present and to scatter. From these data, we extract the rate of photon emission with the procedure described in Section III A. Then, we compare those cascade-rates (using the microscopic rates) to the hydrodynamic rates from equation (5) with the parameters from Table I. Since the available rates in the cascade and hydrodynamic modes differ, as pointed out above, we restrict the comparison to the common rates $\pi\pi \to \gamma\rho$ and $\pi\rho \to \gamma\pi$. The cascade-rates are explicitly summed over all charge combinations.

Figure 5 shows the comparison of the rates at a temperature $T = 150$ MeV. It can be seen that the microscopically obtained rates agree very well with the thermodynamic rates.

B. Photon spectra

Let us now progress to the exploration of the dynamical systems. We split up the evolution of a heavy ion collision in three phases: before, during, and after the hydrodynamic description. Scatterings that happen before the transition to hydrodynamics are dominated by pre-equilibrium effects. Therefore, we denote this phase "pre-equilibrium". In the used setup for $E_{\rm Lab} = 158A$ GeV, this phase takes $t_1 \approx 1.424$ fm [32]. It is the same for every calculation. The second phase is the high-density part of the evolution[**?**]. This is tantamount to an average ending at $t_2 = 13.25$ fm [32]. We call this phase the "hydro" phase or, in the case of pure cascade calculations, the "hot and dense" phase. Finally, all photons that are produced after the transition from hydrodynamics to UrQMD are denoted as "post-freeze-out" or "cold and dilute".

The contributions of each of these phases to the final spectra are shown in Figure 6 for the pure cascade calculation and in Figure 7 for the hybrid calculation with the hadron gas EoS. The black solid lines show the complete direct photon spectra, the green dash-dotted lines show the pre-equilibrium contribution, the red dashed lines show the photon spectrum from the cold and dilute phase and the blue dotted lines show the contribution from the hot and dense stage. In the hybrid model, the evolution during this hot and dense stage is calculated within the hydrodynamic framework. We find that the contribution from the hot and dense phase

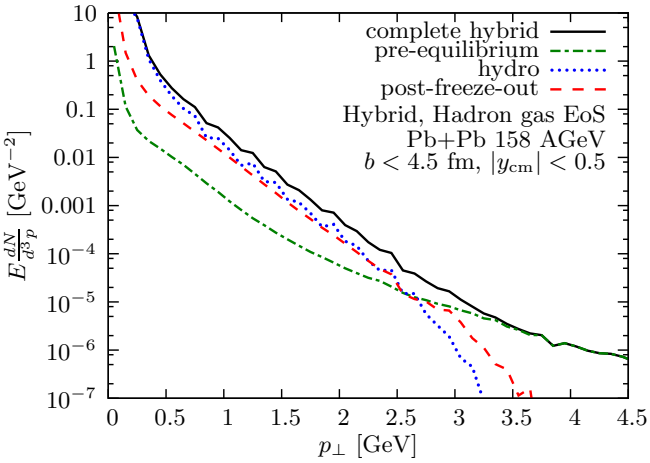

FIG. 7: (Color Online.) Hybrid model calculation with HG-EoS. Contributions of the phases before (green dash-dotted line), during (blue dotted line) and after (red dashed line) the hydrodynamic evolution to the inclusive spectrum (solid black line).

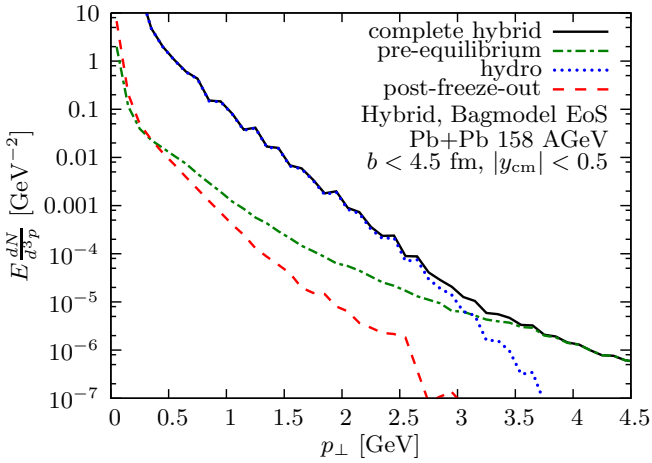

FIG. 8: (Color Online.) Hybrid model calculation with BM-EoS. Contributions to the phases before (green dash-dotted line), during (blue dotted line) and after (red dashed line) the hydrodynamic evolution to the inclusive spectrum (solid black line).

$t_1 = 1.424$ fm $< t < 13.25$ fm $= t_2$ is similar in both models. However, at high transverse momenta $p_\perp > 3$ GeV, the cascade calculation yields more photons from this intermediate time span. This can be related to imperfect thermalization of the system at $t_1 = 1.424$ fm in the initial state, which is forced to thermalization at the transition to the hydrodynamic phase, but preserved when doing cascade-only calculations. However, Figure 6 suggests photon emission towards high transverse momenta from the hot and dense phase is in any case strongly suppressed with respect to photon emission from earlier times. It is therefore justified to neglect non-equilibrium effects from the hot and dense phase in the hybrid model. The major difference between cascade and hybrid model calculations is the magnitude of the contributions from the cold and dilute phase (red dashed lines). Here, both models describe the system in the same way. The contribution from this phase to the hybrid model direct photon spectrum is very similar to the contribution from the hot and dense phase. In the pure cascade calculation, on the contrary, the cold and dilute phase contributes roughly a factor of 5 less to the spectrum than the hot and dense phase does. A possible explanation for this is that the transition procedure from hydrodynamic to transport description enhances the number of meson-meson collisions in the late phase.

Interactions at early times ($t < t_1 = 1.424$ fm) are a significant source of high transverse momentum $p_\perp > 3$ GeV photons. Here, the thermalized system of the later phase provides only minor contributions to the inclusive spectrum.

In the same analysis done for the hybrid model with the bag model EoS (see Fig. 8), the picture is different. The contribution from the hydrodynamic phase is strongly enhanced, and the contribution of the cold and dilute phase

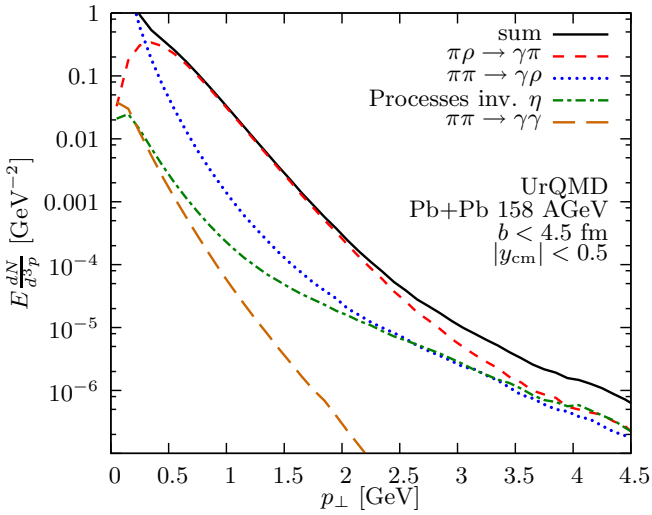

FIG. 9: (Color Online.) UrQMD calculation. Contributions of the different channels.

after the transition from the hydrodynamic phase is, in turn, reduced with respect to the cases presented before. The sum is completely dominated by emission from the hydrodynamic phase at low and intermediate transverse photon momenta $p_\perp < 3$ GeV. This coincides with the observation that the length of the hydrodynamic phase in this model ($t_2 \approx 30$ fm) is much longer than in the calculations with hadron gas EoS ($t_2 \approx 13.25$ fm), due to the large latent heat in the setup with the bag model EoS. At high transverse photon momenta, the early non-equilibrium cascade phase dominate the spectrum.

The contributions of the different channels to the hadronic calculations, both in the pure cascade mode and the hybrid approach with a hadron gas EoS, is shown in Figures 9 and 10. The dominant contributions

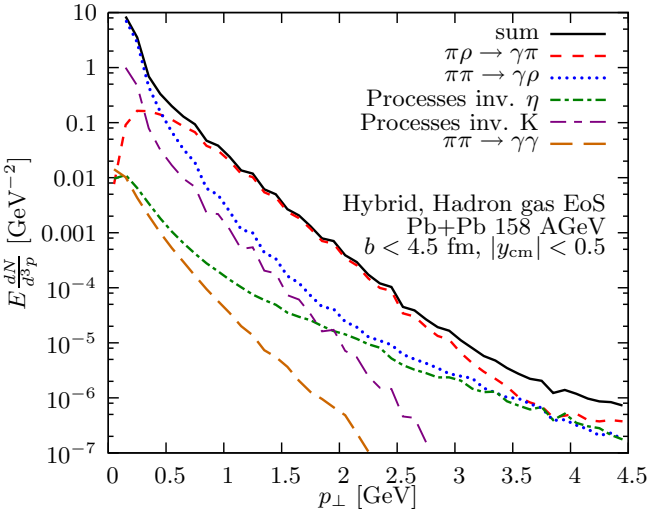

FIG. 10: (Color Online.) Hybrid model calculation with hadron gas EoS. Contributions of the different channels.

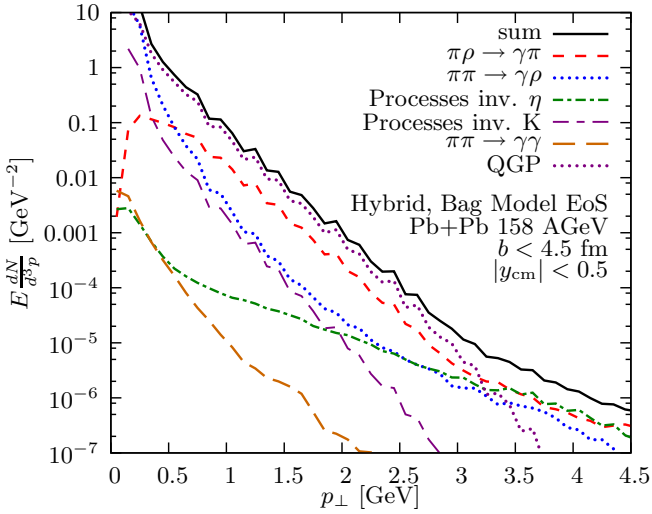

FIG. 11: (Color Online.) Hybrid model calculation with bag model EoS. Contributions of the different channels in hybrid calculation with bag model EoS.

in both models are very similar; at low transverse momenta $p_\perp < 0.5$ GeV, the process with two initial pions $\pi\pi \to \gamma\rho$ is dominant, while in the broad range of 0.5 GeV $< p_\perp <$ 3.5 GeV, $\pi\rho \to \gamma\pi$ is the major source of photons. Processes with an eta-meson ($\pi\pi \to \gamma\eta$ and $\pi\eta \to \gamma\pi$) become important at high transverse momenta, where they contribute in similar magnitude to the two aforementioned channels. Processes with kaons contribute less to the spectrum than the corresponding non-strange channels, and the process $\pi\pi \to \gamma\gamma$ is the least significant in all calculations, as expected.

In the photon spectrum extracted from the cascade calculation, one can observe a flattening of the spectrum at high transverse momenta $p_\perp \approx 3$ GeV. At this point, $\pi\pi \to \gamma\rho$ and η-processes start getting significant. These rates exhibit a flatter slope already at $p_\perp \approx 2$ GeV. In Section IV C, we will show this behaviour to be consistent with the average emission times of the photons at these transverse momenta.

The calculations with the bag model EoS yield a different picture (see Figure 11). Here, the dominant contribution comes from the Quark Gluon Plasma, whose emission magnitude is about two times higher than the combined contribution from all hadronic processes. In contrast, pre-equilibrium hadronic processes are dominant at high transverse momenta $p_\perp > 3$ GeV. Apart from that, we observe a similar distribution among the hadronic channels as we did above (see discussion of Figure 10); the process $\pi\rho \to \gamma\pi$ is dominant in the intermediate $p_\perp$-region, $\pi\pi \to \gamma\rho$ dominates the hadronic contribution at low $p_\perp$, the early scatterings in those channels and the channels involving η-mesons contribute to the high $p_\perp$-region in approximately equal amounts.

A comprehensive comparison between the models presented above and experimental data is shown in Figure 12. Here, we show the sum over all channels and all stages in the cases of pure UrQMD-calculations and

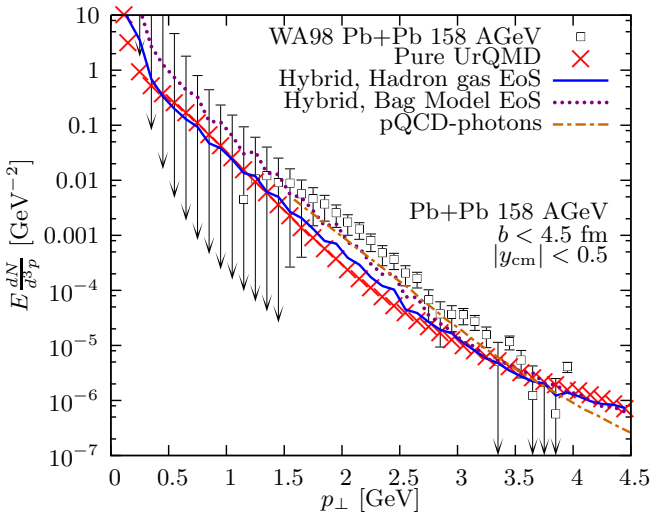

FIG. 12: (Color Online.) Comparison of the direct photon spectra from all variations of the model to the experimental data by the WA98-collaboration [30]. Calculations without intermediate hydrodynamic stage (pure cascade mode) are shown as red crosses, hybrid calculations with hadron gas EoS as red solid line and bag model calculations are depicted by the dark-green dotted line. In addition, we show the contribution from pQCD-photons from [38] (orange dash-dotted line, not included in other lines).

hybrid model with hadron gas and bag model EoS. Also, we show the pQCD-spectrum as presented in [38]. The bag model Equation of State yields the highest photon spectra and provides a reasonable description of the data from the WA98-collaboration [30]. The addition of pQCD-photons following the parametrization of [38] leads to a perfect description of the WA98-data. The purely hadronic calculations, with and without intermediate hydrodynamic calculation, give smaller yields than

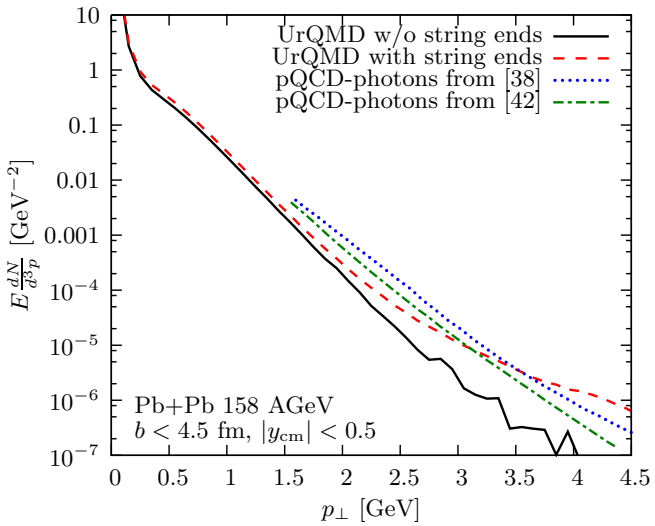

FIG. 13: (Color Online.) UrQMD calculation. Total yields of photons with (solid line) and without (dashed line) the contributions from colliding string ends. For comparison, the spectra of prompt pQCD photons from [38] (dotted line) and [42] (dash-dotted line) are also shown.

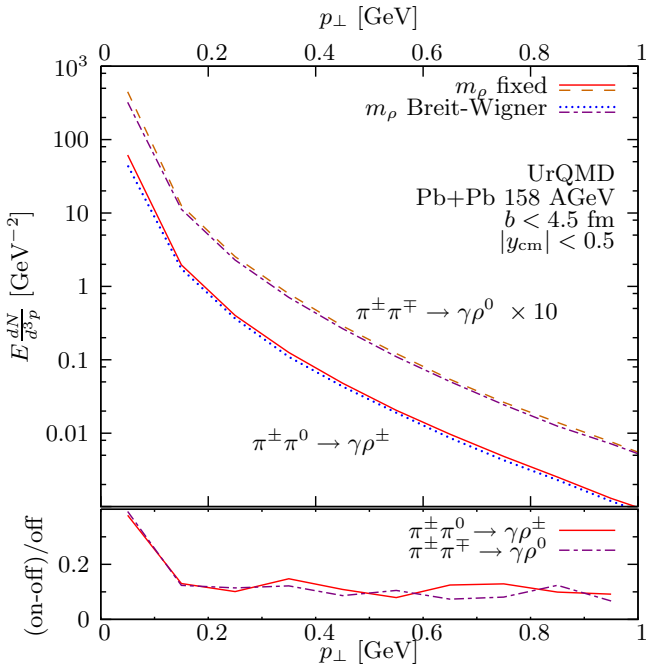

FIG. 14: (Color Online.) UrQMD calculation. Photon spectra from collisions that produce a rho meson in the final state for the production of rho mesons at its pole-mass (solid and dashed lines) and for the production of rho mesons according to a Breit-Wigner-mass distribution (dotted and dash-dotted lines).

the scenario with a QGP. However, when pQCD-photons are added to those calculations, the spectra also come close to the data within the margin of error.

The effects of including the photons from colliding string ends, i.e. interaction of leading (di-)quarks, in the calculation can be seen in Figure 13. The spectrum obtained by neglecting the collision of string ends is exponential and does not exhibit the flattening at high transverse photon momenta. The inclusion of (di-)quark scatterings, however, leads to a strong increase of the photon yield at high $p_\perp$. The contribution of pQCD-photons to the inclusive spectrum starts to be significant already at relatively low transverse photon momenta $p_\perp \approx 1$ GeV, although the magnitude of the contribution differs between the different parametrizations in [38] and [42].

Earlier, we discussed the handling of the rho-meson's finite width. Figure 14 shows the effects of following the calculation outlined there. In both channels, $\pi^\pm\pi^\mp \to \gamma\rho^0$ and $\pi^\pm\pi^0 \to \gamma\rho^\pm$, the yield is about 10 % higher for ρs produced at their pole mass, and only at very low momenta this excess becomes as large as 40 %.

This behaviour can be explained by kinematic arguments: The by far biggest scattering rate in $\pi + \pi$-collisions is at $\sqrt{s} \approx m_\rho^0$. Here, the photon cross-section with fixed pole mass is much higher than the extended calculation with variable rho mass. At all other center-of-mass energies, the extended model gives a higher cross-section, but these rare processes hardly contribute to the spectrum. The processes at low $\sqrt{s}$ will contribute primarily to the low-$p_\perp$-region, because the production of the ρ-meson consumes most of the available energy. Therefore, the enhancement in the model is most pronounced at low $p_\perp$.

We investigate the origin of the change of slope of the spectra at high transverse momenta $p_\perp \approx 3$ GeV in Figures 15, 16 and 17. Two processes may contribute to high $p_\perp$ photons: (I) collisions with a large $\sqrt{s}$ in elementary reactions (i.e. early stage collisions) and (II) collisions of particles with large transverse flow $q_\perp$ but rather small $\sqrt{s}$ (i.e., late stage collisions). To disentangle these effects, we determine the contributions of scatterings with high center-of-mass energy $\sqrt{s} > 4$ GeV and high center-of-mass transverse momentum $q_\perp > 3$ GeV. Figure 15 shows the transverse momentum spectrum of photons. Nearly all photons at high transverse momenta (grey-shaded area) come from collisions with high center-of-mass energies, whereas the contribution of high center-of-mass transverse momenta only shows an trivial structure at $p_\perp \approx q_\perp^{\rm threshold} = 3$ GeV.

One cross-check for Figure 15 is shown in Figure 16. Here, we observe that the collision spectrum is exponential. Only at high transverse boosts, a deviation from an exponential spectrum can be seen. This indicates that most photons with high transverse momentum come from unboosted collisions with $q_\perp < 1$ GeV. The center-of-mass energy and transverse momentum of a collision show no correlation.

The latter can be seen in Figure 17, where the photon production rate is shown as a function of the center-of-mass energy of the individual collisions. The figure confirms the notion that most photons with high transverse

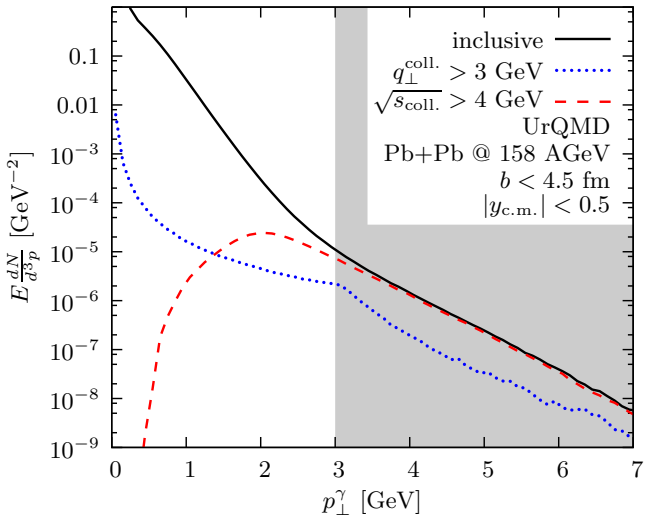

FIG. 15: (Color Online.) UrQMD calculation. The $p_\perp$-spectra for all photons (solid black line), photons from boosted collisions (dotted blue line) and collisions with high center-of-mass energy (dashed red line). The grey-shaded area indicates the range of the $p_\perp$-region used for the solid black lines in Figures 16 and 17.

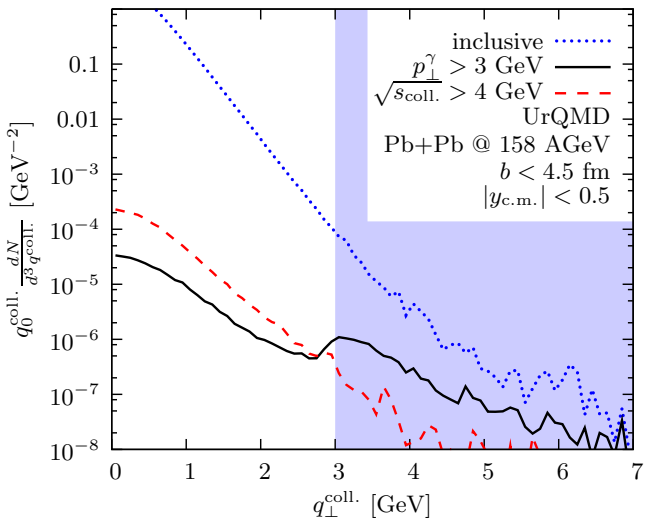

FIG. 16: (Color Online.) UrQMD calculation. The number of photons as a function of the transverse center-of-mass momentum of the elementary collision. We show all photons (blue dotted line), photons that have high transverse momentum (black solid line) and photons from collisions with high center-of-mass energy (red dashed line). The light-blue-shaded area indicates the range of the $q_\perp$-region used for the dotted blue lines in Figures 15 and 17.

momenta come from collisions with high center-of-mass energies. It is worthwhile to observe, however, that starting at $\sqrt{s_{\rm coll.}} = 7$ GeV, each elementary collision produces essentially only photons with transverse momenta $p_\perp > 3$ GeV.

The distribution of center-of-mass energies also shows that the vast majority of collisions happen at the ρ- and

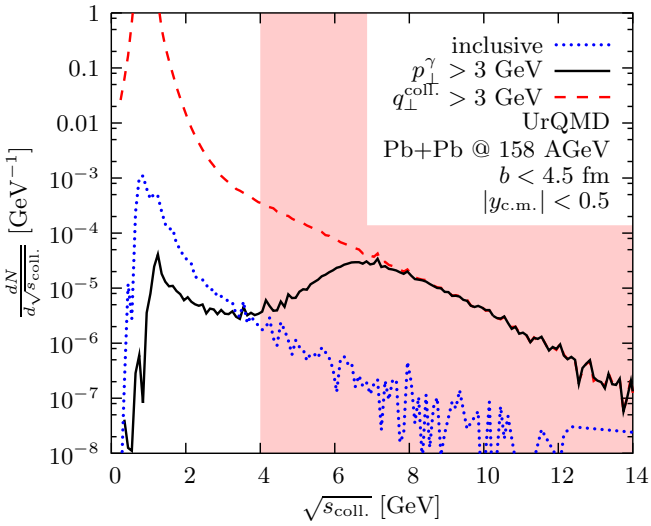

FIG. 17: (Color Online.) UrQMD calculation. The number of photons as a function of the center-of-mass energy of the elementary collision. We show all photons (red dashed line), photons that have high transverse momentum (black solid line) and photons from collisions of with high transverse center-of-mass momentum. The light-red-shaded area shows the range of the $\sqrt{s}$-filter used for the red dashed lines in Figures 15 and 16.

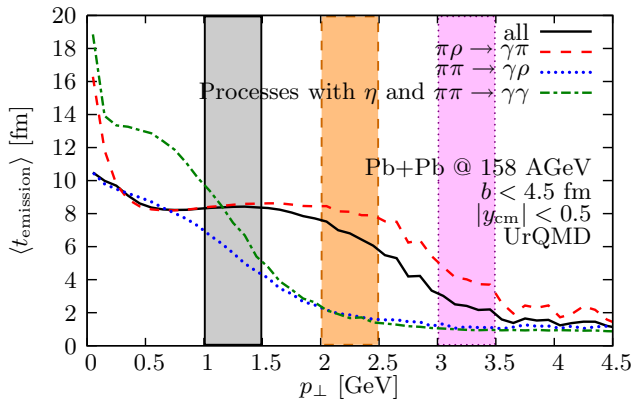

FIG. 18: (Color Online.) UrQMD calculation. Average photon emission times as a function of the transverse momentum for all photons, $\pi\rho \to \gamma\pi$-, $\pi\pi \to \gamma\rho$- and other processes (black solid, red dashed, blue dotted and green dash-dotted lines, respectively). The shaded areas correspond to the $p_\perp$-regions used for the curves shown in Figure 19.

a_1-pole masses.

C. Emission times

In the pure cascade model, we can study the emission times of photons. Figure 18 shows the average emission times of photons as a function of the transverse momentum for the various channels. It is noticeable that over a very broad momentum range, 0.3 GeV $< p_\perp <$ 2.1 GeV,

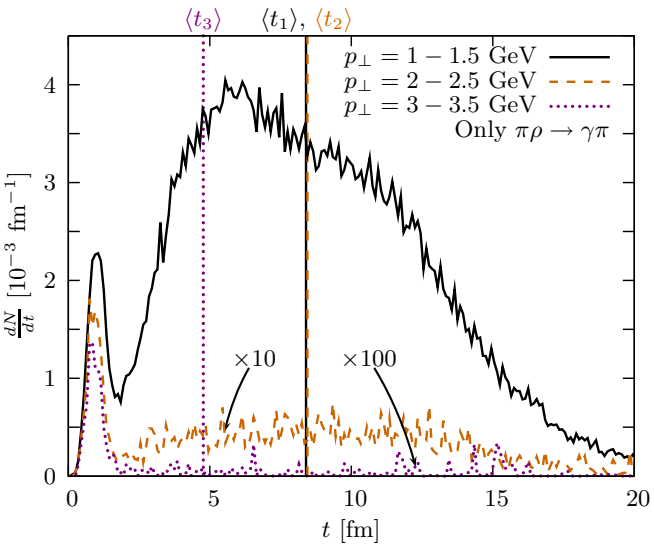

FIG. 19: (Color Online.) UrQMD calculation. Emission time distribution of photons from $\pi\rho$-scatterings for the different photon transverse momentum regions indicated in Figure 18. The vertical lines indicate the average emission time in the corresponding $p_\perp$-bin.

the average emission time stays at a constant level of about $\langle t_{\text{emission}} \rangle \approx 8$ fm. This coincides with the region where the process $\pi\rho \to \gamma\pi$ dominates. Only at high transverse momenta, the early times dominate. This is consistent with the findings in Section IV B, that the spectrum clearly shows two different temperatures, one in the region below $p_\perp = 2.5$ GeV and a different temperature above $p_\perp > 3$ GeV. It also explains why the spectral contributions from $\pi\pi \to \gamma\rho$ and η-processes show a much flatter slope already at $p_\perp \approx 2$ GeV. At late times, when the average center-of-mass energy has decreased, photons are predominantly produced at low transverse momenta.

In Figure 19, we show the emission time distribution of photons in various $p_\perp$-bins for the $\pi\rho \to \gamma\pi$-processes. It is interesting to see that at all transverse momenta, there is an initial flash of photons emitted at very early times $t \approx 1$ fm. In the low $p_\perp$-bin 1 GeV $< p_\perp <$ 1.5 GeV, a very strong contribution from the bulk emission in the hot and dense stage between $t = 4$ fm and $t = 12$ fm raises the average emission time. In the intermediate $p_\perp$-region 2 GeV $< p_\perp <$ 2.5 GeV, bulk contribution is greatly reduced and shines less bright than the initial flash. In the highest $p_\perp$-region 3 GeV $< p_\perp <$ 3.5 GeV, the late bulk contribution is small and the initial stage dominates. However, one should note that due to the long lifetime of the bulk stage, the average emission times are shifted to higher values.

V. SUMMARY

In this work, we have calculated direct photon emission from hadronic and partonic sources. In Section III, we presented our model for photon emission from microscopic collisions (Subsection III A) and from thermal rates (Subsection III B). Then, we introduced the cross-sections and thermal rates used for the present calculations.

Section IV A showed that the emission rates from a thermalized microscopic cascade calculation agree very well with the thermal rates used in the hydrodynamic part of the present model. We discussed the contributions from the different stages before, during and after the high-density part of the evolution to the direct photon spectra for cascade calculations as well as hadron gas and bag model hybrid calculations. The relative contributions of hadron gas hybrid calculation and cascade simulations are similar. However, in the bag model calculations the high-density hydrodynamic phase takes a much longer time and contributes substantially to the photon spectra.

Investigations that differentiate between the different channels showed that the process $\pi\rho \to \gamma\pi$ is the dominant hadronic source for photon production at intermediate photon transverse momenta 0.5 GeV $< p_\perp <$ 3 GeV, while $\pi\pi \to \gamma\rho$ is dominant at low photon transverse momenta $p_\perp <$ 0.5 GeV, only.

When comparing the different variations of the model (see Fig. 12), we found that the hybrid model with a QGP EoS can explain the spectra measured by the WA98-collaboration [30], especially if pQCD-photons are included.

We studied the photon emission from colliding string ends and compared those to pQCD-spectra. The result indicated that direct photon emission from string ends is restricted to the early phase of the collision where the medium is hot. Neglecting those collisions lowers the effective temperature at high transverse momenta $p_\perp >$ 2.5 GeV.

We found that the inclusion of a finite width of the produced ρ-mesons is relevant only at low transverse momenta. I.e., only in the lowest $p_\perp$-bin, the effect of assigning the pole mass or a mass chosen randomly according to the spectral function is important.

We also found that photons at high transverse momenta $p_\perp > 3$ GeV show a significantly flatter slope (and therefore higher effective temperature) than photons with lower $p_\perp$. We attribute this effect to higher center of mass-energies that produce these photons, and we find that it is not significantly influenced by elementary collisions that have a high center of mass-boost in transverse direction. The analysis of average photon emission times showed that photons at $p_\perp > 3$ GeV are emitted significantly earlier than at lower transverse momenta. We find the average emission times of the different channels to be consistent to the contributions of those channels to the complete spectra: The processes $\pi\pi \to \gamma\rho$

and those involving the η-meson show a flat spectrum already at $p_\perp \approx 2$ GeV, and the average emission times from those channels is dominated by the early stage in this momentum region. The process $\pi\rho \to \gamma\pi$, which dominates the spectrum at intermediate $p_\perp$, emits photons at much later times, due to a strong contribution from the bulk evolution.

VI. OUTLOOK

The good agreement between the calculations presented here and the experimental data show that a cascade-hydrodynamic hybrid model can be applied for this kind of calculations. We plan to extend the investigation to a more realistic equation of state with chiral restoration, critical endpoint and rapid cross-over. Also, the decays of short-lived mesons and baryons which cannot be subtracted by the experiment may play a major role in enhancing the direct photon spectra and will therefore be investigated. A major improvement to the model presented here is the direct incorporation of pQCD-processes between initial state-nucleons and the addition of new channels for photon production in the hybrid hydrodynamic and cascade-calculation.

Furthermore, direct photon emission will be studied for the systems studied or planned to be studied at RHIC (PHENIX), LHC (ALICE), FAIR (CBM) and SIS-100 (HADES).

More differential observables like direct photon elliptic flow can also be studied in the aforementioned investigations.

VII. ACKNOWLEDGEMENTS

This work has been supported by the Frankfurt Center for Scientific Computing (CSC), the GSI and the BMBF. The authors thank Hannah Petersen for providing the hybrid- and Dirk Rischke for the hydrodynamic code, as well as Jan Steinheimer-Froschauer for the equation of state. B. Bäuchle gratefully acknowledges support from the Deutsche Telekom Stiftung and the Helmholtz Research School on Quark Matter Studies. This work was supported by the Hessian LOEWE initiative through the Helmholtz International Center for FAIR.

The authors thank Elvira Santini and Pasi Huovinnen for valuable discussions and Klaus Reygers for experimental clarifications.

Appendix A: Differential cross-sections

For completeness, we list the differential cross-sections for the processes used in [8, 9].

$$\frac{d\sigma}{dt}\left(\pi^\pm\pi^\mp \to \gamma\rho^0\right) = \frac{\alpha g_\rho^2}{4sp_{\rm c.m.}^2}\left\{2-(m_\rho^2-4m_\pi^2)\left[\frac{s-2m_\pi^2}{s-m_\rho^2}\frac{1}{t-m_\pi^2}+\frac{m_\pi^2}{(t-m_\pi^2)^2}+(t\leftrightarrow u)\right]\right\} \quad , \tag{A1a}$$

$$\frac{d\sigma}{dt}\left(\pi^\pm\pi^0 \to \gamma\rho^\pm\right) = -\frac{\alpha g_\rho^2}{16sp_{\rm c.m.}^2}\left[\frac{(s-2m_\rho^2)(t-m_\pi^2)^2}{m_\rho^2(s-m_\rho^2)^2}+\frac{(s-6m_\rho^2)(t-m_\pi^2)}{m_\rho^2(s-m_\rho^2)}+\frac{4s(m_\rho^2-4m_\pi^2)}{(s-m_\rho^2)^2}\right.$$
$$\left.+\frac{4(m_\rho^2-4m_\pi^2)}{t-m_\pi^2}\left(\frac{s}{s-m_\rho^2}+\frac{m_\pi^2}{t-m_\pi^2}\right)+\frac{m_\pi^2}{m_\rho^2}-\frac{9}{2}+(t\leftrightarrow u)\right] \quad , \tag{A1b}$$

$$\frac{d\sigma}{dt}\left(\pi^\pm\rho^0 \to \gamma\pi^\pm\right) = \frac{\alpha g_\rho^2}{12sp_{\rm c.m.}^2}\left[2-\frac{s(m_\rho^2-4m_\pi^2)}{(s-m_\pi^2)^2}-\frac{(m_\rho^2-4m_\pi^2)}{t-m_\pi^2}\left(\frac{s-m_\rho^2+m_\pi^2}{(s-m_\pi^2)(t-m_\pi^2)}+\frac{m_\pi^2}{(t-m_\pi^2)}\right)\right] \quad , \tag{A1c}$$

$$\frac{d\sigma}{dt}(\pi^\pm\rho^\mp \to \gamma\pi^0) = -\frac{\alpha g_\rho^2}{48sp_{\rm c.m.}^2}\left\{4(m_\rho^2-4m_\pi^2)\left[\frac{t}{(t-m_\pi^2)^2}+\frac{u}{(u-m_\rho^2)^2}-\frac{m_\rho^2}{s-m_\pi^2}\left(\frac{1}{t-m_\pi^2}+\frac{1}{u-m_\rho^2}\right)\right]\right.$$
$$\left.+\left(3+\frac{s-m_\pi^2}{m_\rho^2}\right)\frac{s-m_\pi^2}{u-m_\rho^2}-\frac{1}{2}+\frac{s}{m_\rho^2}-\left(\frac{s-m_\pi^2}{u-m_\rho^2}\right)^2\right\} \quad , \tag{A1d}$$

$$\frac{d\sigma}{dt}\left(\pi^0\rho^\pm \to \gamma\pi^\pm\right) = \frac{\alpha g_\rho^2}{48sp_{\rm c.m.}^2}\left[\frac{9}{2}-\frac{s}{m_\rho^2}-\frac{4s(m_\rho^2-4m_\pi^2)}{(s-m_\pi^2)^2}+\frac{(s-m_\pi^2)^2-4m_\rho^2(m_\rho^2-4m_\pi^2)}{(u-m_\rho^2)^2}\right.$$
$$\left.+\frac{1}{u-m_\rho^2}\left(5(s-m_\pi^2)-\frac{(s-m_\pi^2)^2}{m_\rho^2}-\frac{4(m_\rho^2-4m_\pi^2)(s-m_\pi^2+m_\rho^2)}{s-m_\pi^2}\right)\right] \quad , \tag{A1e}$$

$$\frac{d\sigma}{dt}\left(\pi^\pm\pi^\mp \to \gamma\eta\right) = \frac{\pi\alpha A\left|F_\pi(s)\right|^2}{16m_\eta^2m_\rho^4sp_{\rm c.m.}^2}\left[s(u-m_\pi^2)(t-m_\pi^2)-m_\pi^2(s-m_\eta^2)^2\right] \quad , \tag{A1f}$$

$$\frac{d\sigma}{dt}\left(\pi^\pm\eta \to \gamma\pi^\pm\right) = \frac{\pi\alpha A\left|F_\pi(u)\right|^2}{16m_\eta^2m_\rho^4sp_{\rm c.m.}^2}\left[u(s-m_\pi^2)(t-m_\pi^2)-m_\pi^2(u-m_\eta^2)^2\right] \quad , \tag{A1g}$$

$$\frac{d\sigma}{dt}\left(\pi^\pm\pi^\mp \to \gamma\gamma\right) = \frac{2\pi\alpha^2}{sp_{\rm c.m.}^2}\left[1+2m_\pi^2\left(\frac{1}{t-m_\pi^2}+\frac{1}{u-m_\pi^2}\right)+2m_\pi^4\left(\frac{1}{t-m_\pi^2}+\frac{1}{u-m_\pi^2}\right)^2\right] \quad . \tag{A1h}$$

In these equations, $t = (p_\pi - p_\gamma)^2$ is always the momentum transfer from the pion to the photon[**?**] (unlike the convention used in [8]) and $p_{\rm c.m.} = (2\sqrt{s})^{-1}\sqrt{s^2-2s(m_1^2+m_2^2)+(m_1^2-m_2^2)^2}$ is the three-momentum of the incoming particles in the center-of-mass frame (m_1 and m_2 being their masses). The value of A is, consistent with [8], $A = g_{\eta\rho\rho}^2 g_\rho^2/4\pi\gamma_\rho^2 = 4.7$, and the pion electromagnetic form factor is

$$F_\pi(s) = \frac{m_\rho^4}{(s-m_\rho^2)+\Gamma_\rho^2 m_\rho^2} \quad .$$

In their 1992 paper, Xiong *et al.* [9] calculate the cross-section for the formation of an intermediate a_1-meson during $\pi\rho$-scattering, averaged over all possible charge combinations:

$$\frac{d\sigma}{dt}\left(\pi\rho \to a_1 \to \gamma\pi\right) = \frac{\pi^2\sqrt{s}}{2p_{\rm c.m.}^3(s-m_\pi)^2}\frac{\Gamma_{a_1\to\pi\rho}\Gamma_{a_1\to\gamma\pi}}{(\sqrt{s}-m_{a_1})^2+(\Gamma_{a_1\to\pi\rho}+\Gamma_{a_1\to\gamma\pi})^2/4} \quad . \tag{A1i}$$

This channel is not included in Kapusta *et al.* Xiong *et al.* obtain this from a Lagrange-density involving only the pion-, photon-, rho- and a_1-fields

$$\mathcal{L} = G_\rho a_1^\mu (g_{\mu\nu}(p_\pi \cdot p_\rho) - p_{\pi\mu} p_{\rho\nu})\rho^\nu \Phi + G_\rho \frac{e}{g_\rho} a_1^\mu (g_{\mu\nu}(p_\pi \cdot p_\gamma) - p_{\pi\mu} p_{\gamma\nu}) A^\nu \Phi \quad , \tag{A2}$$

where $G_\rho = 14.8$ GeV^{-1}. The partial widths of the a_1, $\Gamma_{a_1 \to \pi\rho}$ and $\Gamma_{a_1 \to \gamma\pi}$, are estimated to be

$$\Gamma_{a_1 \to \pi\rho} = \frac{G_\rho^2 p_{\text{c.m.}}}{24\pi m_{a_1}^2} \left\{ \frac{m_\rho^2}{4s} \left[s - (m_\rho^2 - m_\pi^2) \right] + \frac{1}{2}(s - m_\rho^2 - m_\pi^2) \right\} \quad \text{and} \tag{A3a}$$

$$\Gamma_{a_1 \to \gamma\pi} = \frac{G_\rho^2 \alpha p_{\text{c.m.}}}{12 g_\rho^2 m_{a_1}^2} (s - m_\pi^2) \quad . \tag{A3b}$$

Appendix B: Integrated Cross-sections

The integration over the cross-sections listed in appendix A yield the following results:

$$\sigma\left(\pi^{\pm}\pi^{\mp}\to\gamma\rho^{0}\right) = \frac{\alpha g_{\rho}^{2}}{4sp_{\rm c.m.}^{2}}\left\{2\Delta t-(m_{\rho}^{2}-4m_{\pi}^{2})\left[\frac{s-2m_{\pi}^{2}}{s-m_{\rho}^{2}}\ln\frac{(t_{-}-m_{\pi}^{2})}{(t_{+}-m_{\pi}^{2})}\right.\right.$$
$$\left.\left.+\frac{m_{\pi}^{2}\Delta t}{(m_{\pi}^{2}-t_{+})(m_{\pi}^{2}-t_{-})}+(t_{\pm}\leftrightarrow u_{\mp})\right]\right\}\quad, \tag{B1a}$$

$$\sigma\left(\pi^{\pm}\pi^{0}\to\gamma\rho^{\pm}\right) = -\frac{\alpha g_{\rho}^{2}}{16sp_{\rm c.m.}^{2}}\left[\frac{s-2m_{\rho}^{2}}{m_{\rho}^{2}(s-m_{\rho}^{2})^{2}}\frac{1}{3}(t_{-}^{3}-t_{+}^{3})+\frac{s-6m_{\rho}^{2}}{m_{\rho}^{2}(s-m_{\rho}^{2})}\frac{1}{2}(t_{-}^{2}-t_{+}^{2})\right.$$
$$+\left(\frac{4s(m_{\rho}^{2}-4m_{\pi}^{2})}{(s-m_{\rho}^{2})^{2}}+\frac{m_{\pi}^{2}}{m_{\rho}^{2}}-\frac{9}{2}\right)\Delta t+\frac{4s(m_{\rho}^{2}-4m_{\pi}^{2})}{(s-m_{\rho}^{2})}\ln\frac{t_{-}-m_{\pi}^{2}}{t_{+}-m_{\pi}^{2}}$$
$$\left.+\frac{4m_{\pi}^{2}(m_{\rho}^{2}-4m_{\pi}^{2})\Delta t}{(m_{\pi}^{2}-t_{+})(m_{\pi}^{2}-t_{-})}+(t_{\pm}\leftrightarrow u_{\mp})\right]\quad, \tag{B1b}$$

$$\sigma\left(\pi^{\pm}\rho^{0}\to\gamma\pi^{\pm}\right) = \frac{\alpha g_{\rho}^{2}}{12sp_{\rm c.m.}^{2}}\left[2\Delta t-\frac{s(m_{\rho}^{2}-4m_{\pi}^{2})}{(s-m_{\pi}^{2})^{2}}\Delta t-(m_{\rho}^{2}-4m_{\pi}^{2})\left(\frac{s-m_{\rho}^{2}+m_{\pi}^{2}}{s-m_{\pi}^{2}}\ln\frac{t_{-}-m_{\pi}^{2}}{t_{+}-m_{\pi}^{2}}\right.\right.$$
$$\left.\left.+\frac{m_{\pi}^{2}\Delta t}{(m_{\pi}^{2}-t_{+})(m_{\pi}^{2}-t_{-})}\right)\right]\quad, \tag{B1c}$$

$$\sigma(\pi^{\pm}\rho^{\mp}\to\gamma\pi^{0}) = -\frac{\alpha g_{\rho}^{2}}{48sp_{\rm c.m.}^{2}}\left\{4(m_{\rho}^{2}-4m_{\pi}^{2})\left[\frac{m_{\pi}^{2}\Delta t}{(u_{+}-m_{\rho}^{2})(u_{-}-m_{\rho}^{2})}+\frac{m_{\pi}^{2}\Delta t}{(t_{+}-m_{\pi}^{2})(t_{-}-m_{\pi}^{2})}\right.\right.$$
$$\left.+\ln\frac{u_{+}-m_{\rho}^{2}}{u_{-}-m_{\rho}^{2}}+\ln\frac{t_{-}-m_{\pi}^{2}}{t_{+}-m_{\pi}^{2}}-\frac{m_{\rho}^{2}}{s-m_{\pi}^{2}}\left(\ln\frac{t_{-}-m_{\pi}^{2}}{t_{+}-m_{\pi}^{2}}+\ln\frac{u_{+}-m_{\rho}^{2}}{u_{-}-m_{\rho}^{2}}\right)\right]$$
$$\left.+(s-m_{\pi}^{2})\left(3+\frac{s-m_{\pi}^{2}}{m_{\rho}^{2}}\right)\ln\frac{u_{+}-m_{\rho}^{2}}{u_{-}-m_{\rho}^{2}}+\Delta t\left(\frac{s}{m_{\rho}^{2}}-\frac{1}{2}-\frac{(s-m_{\pi}^{2})^{2}}{(u_{+}-m_{\rho}^{2})(u_{-}-m_{\rho}^{2})}\right)\right\}\quad, \tag{B1d}$$

$$\sigma\left(\pi^{0}\rho^{\pm}\to\gamma\pi^{\pm}\right) = \frac{\alpha g_{\rho}^{2}}{48sp_{\rm c.m.}^{2}}\left[\Delta t\left(\frac{9}{2}-\frac{s}{m_{\rho}^{2}}-\frac{4s(m_{\rho}^{2}-4m_{\pi}^{2})}{(s-m_{\pi}^{2})^{2}}+\frac{(s-m_{\pi}^{2})^{2}-4m_{\rho}^{2}(m_{\rho}^{2}-4m_{\pi}^{2})}{(u_{+}-m_{\rho}^{2})(u_{-}-m_{\rho}^{2})}\right)\right.$$
$$\left.+\left(5(s-m_{\pi}^{2})-\frac{(s-m_{\pi}^{2})^{2}}{m_{\rho}^{2}}-\frac{4(m_{\rho}^{2}-4m_{\pi}^{2})(s-m_{\pi}^{2}+m_{\rho}^{2})}{s-m_{\pi}^{2}}\right)\ln\frac{u_{+}-m_{\rho}^{2}}{u_{-}-m_{\rho}^{2}}\right]\quad, \tag{B1e}$$

$$\sigma\left(\pi^{\pm}\pi^{\mp}\to\gamma\eta\right) = \frac{\pi\alpha A\left|F_{\pi}(s)\right|^{2}}{16m_{\eta}^{2}m_{\rho}^{4}sp_{\rm c.m.}^{2}}\left[(2m_{\pi}^{2}+m_{\eta}^{2}-s)\frac{s}{2}(t_{+}^{2}-t_{-}^{2})-\frac{s}{3}(t_{+}^{3}-t_{-}^{3})-m_{\pi}^{2}\left(m_{\eta}^{4}+s(m_{\pi}^{2}-m_{\eta}^{2})\right)\right] \tag{B1f}$$

$$\sigma\left(\pi^{\pm}\eta\to\gamma\pi^{\pm}\right) = \frac{\pi\alpha A}{16m_{\eta}^{2}sp_{\rm c.m.}^{2}}\left\{-m_{\pi}^{2}\left[(t_{-}+u_{-})(s-m_{\pi}^{2})+(2m_{\pi}^{2}-s)^{2}\right]I_{0}\right.$$
$$+\left[(s-m_{\pi}^{2})(m_{\pi}^{2}+t_{-}+u_{-})-2m_{\pi}^{2}(s-2m_{\pi}^{2})\right]\left[(t_{-}+u_{-}-m_{\rho}^{2})I_{0}+\frac{1}{2}I_{1}\right]$$
$$\left.-s\left[\Delta t+(t_{-}+u_{-}-m_{\rho}^{2})I_{1}+(t_{-}+u_{-}-m_{\rho}^{2})^{2}I_{0}-m_{\rho}^{2}\Gamma_{\rho}^{2}I_{0}\right]\right\}\quad, \tag{B1g}$$

$$\sigma\left(\pi^{\pm}\pi^{\mp}\to\gamma\gamma\right) = \frac{2\pi\alpha^{2}}{sp_{\rm c.m.}^{2}}\left\{\Delta t+2m_{\pi}^{2}\left[\left(1-\frac{2m_{\pi}^{2}}{s}\right)\ln\frac{t_{-}-m_{\pi}^{2}}{t_{+}-m_{\pi}^{2}}+\frac{m_{\pi}^{2}\Delta t}{(t_{-}-m_{\pi}^{2})(t_{+}-m_{\pi}^{2})}+(t_{\pm}\leftrightarrow u_{\mp})\right]\right\} \tag{B1h}$$

$$\sigma\left(\pi\rho\to a_{1}\to\gamma\pi\right) = 4p_{1}\omega\frac{d\sigma}{dt}\left(\pi\rho\to a_{1}\to\gamma\pi\right)\quad. \tag{B1i}$$

In those equations, $t_{\pm}=m_{1}^{2}-2\omega(E_{1}\pm p_{1})$ are the minimal and maximal allowed momentum transfers, and correspondingly $u_{\pm}=m_{1}^{2}+m_{2}^{2}+m_{4}^{2}-s-t_{\pm}$, and Δt is a shorthand for $t_{-}-t_{+}$. The indices 1, 2 and 4 denote the particles in the order given on the left hand side of the equations (3 is the photon). E_{1}, p_{1} and $\omega=E_{3}$ denote momentum and energy of the respective particles in the center-of-mass frame. In the cross-section $\pi^{\pm}\eta\to\gamma\pi^{\pm}$ (Eq. (B1g)), the following notations have been used for simplicity:

$$I_0 = \frac{1}{m_\rho \Gamma_\rho}\left[\mathrm{atan}\left(\frac{u_+ - m_\rho^2}{m_\rho \Gamma_\rho}\right) - \mathrm{atan}\left(\frac{u_- - m_\rho^2}{m_\rho \Gamma_\rho}\right)\right] \quad \text{and} \tag{B2a}$$

$$I_1 = \ln\left(\frac{(u_- - m_\rho^2)^2 + m_\rho^2\Gamma_\rho^2}{(u_+ - m_\rho^2)^2 + m_\rho^2\Gamma_\rho^2}\right) \quad . \tag{B2b}$$

[1] J. W. Harris and B. Muller, Ann. Rev. Nucl. Part. Sci. **46** (1996) 71 [arXiv:hep-ph/9602235].

[2] S. A. Bass, M. Gyulassy, H. Stoecker and W. Greiner, J. Phys. G **25** (1999) R1 [arXiv:hep-ph/9810281].

[3] J. Adams *et al.* [STAR Collaboration], Nucl. Phys. A **757** (2005) 102 [arXiv:nucl-ex/0501009].

[4] B. B. Back *et al.*, Nucl. Phys. A **757** (2005) 28 [arXiv:nucl-ex/0410022].

[5] I. Arsene *et al.* [BRAHMS Collaboration], Nucl. Phys. A **757** (2005) 1 [arXiv:nucl-ex/0410020].

[6] K. Adcox *et al.* [PHENIX Collaboration], Nucl. Phys. A **757** (2005) 184 [arXiv:nucl-ex/0410003].

[7] C. Alt *et al.* [NA49 Collaboration], Phys. Rev. C **77** (2008) 024903 [arXiv:0710.0118 [nucl-ex]].

[8] J. I. Kapusta, P. Lichard and D. Seibert, Phys. Rev. D **44** (1991) 2774 [Erratum-ibid. D **47** (1993) 4171].

[9] L. Xiong, E. V. Shuryak and G. E. Brown, Phys. Rev. D **46** (1992) 3798 [arXiv:hep-ph/9208206].

[10] S. A. Bass *et al.*, Prog. Part. Nucl. Phys. **41** (1998) 255 [Prog. Part. Nucl. Phys. **41** (1998) 225] [arXiv:nucl-th/9803035].

[11] M. Bleicher *et al.*, J. Phys. G **25** (1999) 1859 [arXiv:hep-ph/9909407].

[12] D. Molnar and P. Huovinen, Phys. Rev. Lett. **94** (2005) 012302 [arXiv:nucl-th/0404065].

[13] Z. Xu and C. Greiner, Phys. Rev. C **71** (2005) 064901 [arXiv:hep-ph/0406278].

[14] Z. W. Lin, C. M. Ko, B. A. Li, B. Zhang and S. Pal, Phys. Rev. C **72** (2005) 064901 [arXiv:nucl-th/0411110].

[15] G. Burau, J. Bleibel, C. Fuchs, A. Faessler, L. V. Bravina and E. E. Zabrodin, Phys. Rev. C **71** (2005) 054905 [arXiv:nucl-th/0411117].

[16] H. W. Barz and B. Kampfer, Nucl. Phys. A **683** (2001) 594 [arXiv:nucl-th/0005063].

[17] A. B. Larionov, O. Buss, K. Gallmeister and U. Mosel, Phys. Rev. C **76** (2007) 044909 [arXiv:0704.1785 [nucl-th]].

[18] J. Bleibel, G. Burau, A. Faessler and C. Fuchs, Phys. Rev. C **76** (2007) 024912 [arXiv:nucl-th/0610021].

[19] J. Bleibel, G. Burau and C. Fuchs, Phys. Lett. B **659** (2008) 520 [arXiv:0711.3366 [nucl-th]].

[20] D. H. Rischke, Y. Pursun and J. A. Maruhn, Nucl. Phys. A **595** (1995) 383 [Erratum-ibid. A **596** (1996) 717] [arXiv:nucl-th/9504021].

[21] T. Hirano, Phys. Rev. C **65** (2002) 011901 [arXiv:nucl-th/0108004].

[22] P. Huovinen, M. Belkacem, P. J. Ellis and J. I. Kapusta, Phys. Rev. C **66** (2002) 014903 [arXiv:nucl-th/0203023].

[23] P. F. Kolb and U. W. Heinz, arXiv:nucl-th/0305084.

[24] C. Nonaka and S. A. Bass, Phys. Rev. C **75** (2007) 014902 [arXiv:nucl-th/0607018].

[25] K. Dusling and D. Teaney, Phys. Rev. C **77** (2008) 034905 [arXiv:0710.5932 [nucl-th]].

[26] R. Baier, P. Romatschke and U. A. Wiedemann, Phys. Rev. C **73** (2006) 064903 [arXiv:hep-ph/0602249].

[27] H. Song and U. W. Heinz, Phys. Rev. C **78** (2008) 024902 [arXiv:0805.1756 [nucl-th]].

[28] A. Dumitru, M. Bleicher, S. A. Bass, C. Spieles, L. Neise, H. Stoecker and W. Greiner, Phys. Rev. C **57** (1998) 3271 [arXiv:hep-ph/9709487].

[29] E. L. Bratkovskaya, S. M. Kiselev and G. B. Sharkov, Phys. Rev. C **78** (2008) 034905 [arXiv:0806.3465 [nucl-th]].

[30] M. M. Aggarwal *et al.* [WA98 Collaboration], arXiv:nucl-ex/0006007.

[31] T. Sjostrand, S. Mrenna and P. Skands, JHEP **0605** (2006) 026 [arXiv:hep-ph/0603175].

[32] H. Petersen, J. Steinheimer, G. Burau, M. Bleicher and H. Stocker, Phys. Rev. C **78** (2008) 044901 [arXiv:0806.1695 [nucl-th]].

[33] J. Steinheimer, M. Mitrovski, T. Schuster, H. Petersen, M. Bleicher and H. Stoecker, arXiv:0811.4077 [hep-ph].

[34] H. Petersen, M. Mitrovski, T. Schuster and M. Bleicher, arXiv:0903.0396 [hep-ph].

[35] Q. f. Li, J. Steinheimer, H. Petersen, M. Bleicher and H. Stocker, Phys. Lett. B **674** (2009) 111 [arXiv:0812.0375 [nucl-th]].

[36] H. Petersen, J. Steinheimer, M. Bleicher and H. Stocker, J. Phys. G **36** (2009) 055104 [arXiv:0902.4866 [nucl-th]].

[37] H. Petersen, J. Steinheimer, G. Burau and M. Bleicher,

[38] S. Turbide, R. Rapp and C. Gale, Phys. Rev. C **69** (2004) 014903 [arXiv:hep-ph/0308085].

[39] F. Arleo *et al.*, arXiv:hep-ph/0311131.

[40] F. M. Liu and K. Werner, J. Phys. G **36** (2009) 035101 [arXiv:0712.3619 [hep-ph]].

[41] P. Arnold, G. D. Moore and L. G. Yaffe, JHEP **0112** (2001) 009 [arXiv:hep-ph/0111107].

[42] C. Gale, Nucl. Phys. A **698** (2002) 143 [arXiv:hep-ph/0104235].

[43] C. Y. Wong and H. Wang, Phys. Rev. C **58** (1998) 376 [arXiv:hep-ph/9802378].

[] In the pure cascade mode, we define it to be as long as the average length of the hydrodynamic phase when running with the hadron gas EoS.

[] All cases with two pions in the initial state are symmetric in $t \leftrightarrow u$. Therefore, it is not necessary to specify which pion is the reference for t.